Available online at www.sciencedirect.com

ScienceDirect

Procedia Manufacturing 51 (2020) 870–877

Procedia MANUFACTURING

www.elsevier.com/locate/procedia

30th International Conference on Flexible Automation and Intelligent Manufacturing (FAIM2021)
15-18 June 2021, Athens, Greece.

Numerical simulation of adhesively-bonded *T*-stiffeners by cohesive zone models

J.A.M. Ferreira[a], R.D.S.G. Campilho[a,b,*], M.G. Cardoso[a,c], F.J.G. Silva[a]

[a]*Departamento de Engenharia Mecânica, Instituto Superior de Engenharia do Porto, Instituto Politécnico do Porto, Rua Dr. António Bernardino de Almeida, 431, 4200-072 Porto, Portugal*

[b]*INEGI – Pólo FEUP, Rua Dr. Roberto Frias, s/n, 4200-465 Porto, Portugal*

[c]*Departamento de Engenharia Mecânica, Faculdade de Engenharia da Universidade do Porto, Rua Dr. Roberto Frias, s/n, 4200-465 Porto, Portugal*

* Corresponding author. Tel.: +351 939 526 892; fax: +351-228-321-159. *E-mail address:* raulcampilho@gmail.com

Abstract

Nowadays, the adhesive bonding method has a strong presence in the most varied industries. The bonding of composite materials with structural adhesives became more relevant in the industry, such as the aeronautical industry, which takes advantage of stiffener structures in composite materials using adhesive bonds. In any area of industry, large-scale application of a particular bonding technique requires reliable tools for the design and prediction of failure. This work evaluates the performance of a structural adhesive (Araldite® 2015) on a *T*-stiffener with composite adherends composed of an epoxy matrix reinforced with carbon fibers. The aim of the work is to numerically study, by the Finite Element Method (FEM) and Cohesive Zone Models (CZM), the behavior of different *T*-stiffener configurations under peel loads. A parametric study was carried out, including elastic stress analysis and maximum load (P_m) prediction, considering four geometrical parameters: flat adherend thickness (t_P), stiffener thickness (t_0), overlap length (L_O) and curved deltoid radius (R). A significant effect was found for all studied parameters, on both stress distributions and P_m, enabling to define the optimal joint parameters for the *T*-stiffeners.

Keywords: Structural adhesive; adhesive joint; *T*-stiffener; cohesive zone model.

1. Introduction

There has been a growing application of adhesive joints in all industries, such as aeronautics, automotive and shipbuilding. To join two or more components, three technologies cover the vast majority of situations: bolted and riveted joints, welded joints, and adhesive joints. Adhesive joints are becoming increasingly relevant due to advantages such as ease of fabrication, uniformity of stress distributions over the joint width and ability to join different materials [1]. There are several ways to classify an adhesive. In the industry, adhesives are typically characterized by its performance and divided into two distinct groups: structural and non-structural [2]. Structural adhesives are adhesives that have long life and shear strength of more than 7 MPa [3]. Structural adhesive bonds are widely used mainly in high added-value industries, where there is a large use of composite materials, such as aeronautics, marine, automotive, among others. Generally, adhesive applications are used together with composite materials, which evolved mainly with the development of synthetic polymers in the twentieth century. Actually, the use of welded bonds in these materials is unviable and mechanical bonds cause discontinuity of the fibres at the drilled holes, causing the up rise of adhesive joints [4].

Several techniques can be used to predict the strength of adhesive joints. These techniques are divided into two major groups: analytical and numerical models. With the increasing use of adhesive bonds, the industry needs tools to predict the strength of structures with these bonds. When carrying out projects or for scientific study, it is important to make a reliable

10.1016/j.promfg.2020.10.122

numerical study, which simulates the real loading conditions. The main existing numerical techniques are continuum mechanics, fracture mechanics, CZM, damage mechanics and the eXtended Finite Element Method (XFEM) [5, 6]. These can be used together with theoretical or numerical methods such as the FEM. Continuum mechanics techniques consist of estimating the stress distributions in the adhesive, and using selected strength or strain-based criteria to evaluate failure [7]. In this topic, the FEM deals better with complex structures and non-linear materials [8]. Although fracture mechanics is not common in adhesive joints, the Virtual Crack Closing Technique (VCCT) is still used (for example [9, 10]). CZM uses the principles of strength of materials to infer damage initiation, and fracture mechanics to predict the propagation of damage, thus providing the complete response of damage to structural failure [11, 12]. Different works have shown that this technique is accurate if the laws of CZM are correctly estimated [13]. XFEM is a recent evolution of FEM, which allows modelling damage growth, based on the strength of materials for the initiation of damage and strains for the evaluation of fracture. Compared to CZM models, in XFEM it is no longer necessary for the crack to follow a pre-defined path, which is a significant advantage. Thus, the crack can propagate freely within the structure without the need for the mesh to coincide with the geometry of the discontinuities and without the need to redo the mesh in the vicinity of the crack [14]. Despite the availability of all these techniques, CZM are the most used to predict the strength of adhesive joints [15].

Stiffeners are thin plate (skin) reinforcements to provide higher stiffness. Although several stiffener configurations are available, one of the most common is the stiffener in flat bar connected with a *T*-joint. The research of de Freitas and Sinke [16] evaluated the performance of two adhesively-bonded stiffener skin connections. Two stiffeners were analysed: one made of glass-fibre reinforced plastics (GFRP) composite and another with aluminium stiffener, bonded to a fibre metal laminate (FML) skin. The adhesive joints were tested using stiffener pull-off tests (SPOT), which is a typical configuration used to simulate the structural behaviour of large-scale components subject to off-plane loading, such as the internal pressure of a fuselage or a low pressure zone of the leading edge. In the hybrid joint (composite stiffener and FML), damage begins at the central zone of the composite stiffener. An unstable delamination arises, which propagates from the centre of the stiffener to the end through the interlaminar stiffener layers (> 90% of failure is inter/intralaminar) and, in limited areas, damage occurs in the adhesive (<10% failure in the adhesive). In the metal joint, failure begins in the adhesive at the overlap ends. Unstable tear propagates from the ends to the centre of the overlap. Complete failure occurs in the adhesive (100% cohesive failure). The P_m associated to the composite stiffener is 40 to 60% less than P_m of the joint with aluminium stiffener. The research identified that, to use the full capacity of hybrid adhesive joints, the adhesion between the carbon fibres of the laminate and the intralaminar strength must be improved in order to compete with the most efficient aluminium stringers. Shenoi and Violette [17] examined the influence of *T*-joint geometry on the ability to transfer out-of-plane loads to a hull bulkhead joint. In small vessels, these bulkheads are stiffener structures that contribute to the overall stiffness of the hull and deck assembly, where the hull has to retain its shape after loading. Three typical *T*-joint geometries are used in shipbuilding and these authors have studied five different joints taking these typical geometries into account. The obtained results showed that the optimum radius of the filler fillet should be chosen so that the radius comes out approximately the thickness of the sandwich panel, to correlate with empirical formulas used in epoxy wood construction. If weight criteria are not so important, i.e. for a monochrome structure with a small number of bulkheads and beams, the foam filling performs better from a strength point of view, but it should only be used if skilled workers and a large construction budget are available. The numerical models showed slightly higher P_m than the tests due to the non-consideration of manufacturing defects [17].

This work evaluates the performance of a structural adhesive (Araldite® 2015) on a *T*-stiffener with composite adherends composed of an epoxy matrix reinforced with carbon fibres. The aim of the work is to numerically study, by the FEM and CZM, the behaviour of different *T*-stiffener configurations under peel loads. A parametric study was carried out, including elastic stress analysis and P_m prediction, considering four geometrical parameters: t_P, t_0, L_O and R.

2. Experimental analysis

2.1. Joint geometry

This study analyses a *T*-joint, representing a stiffener, whose geometry is shown in Fig. 1. The base dimensions employed in this work are the following (in mm): width B=20, specimen length L_T=200, curved element free length L_A=30, L_O=30, t_P=3, t_0=1.5, R=6 and adhesive thickness t_A=0.2. A numerical study was performed on the geometric influence of the most relevant dimensional parameters: t_P (1, 2, 3 and 4 mm), t_0 (0.5, 1, 1.5, 2 and 2.5 mm), R (3, 6, 9, 12 mm) and L_O (10, 20, 30, 40 mm).

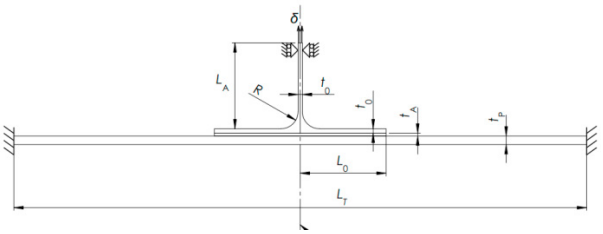

Fig. 1 – Stiffener geometry and dimensions

2.2. Materials

The adherends used in this work are composite pre-impregnated unidirectional CFRP plates with epoxy matrix (SEAL® Texipreg HS 160 RM; Legnano, Italy) with ply thickness of 0.125 mm, and fabricated by manual lay-up and hot-plates press curing for 1 h at 130°C and pressure 2 bar. According to the manufacturer, for the indicated conditions the fibre volume fraction is approximately 64%. The elastic orthotropic properties of a unidirectional lamina for identical curing conditions are indicated in Table 1 [18].

Table 1- Elastic orthotropic properties of a unidirectional carbon-epoxy ply aligned in the fibres direction (*x*-direction; *y* and *z* are the transverse and through-thickness directions, respectively) [18].

E_x=1.09E+05 MPa	ν_{xy}=0.342	G_{xy}=4315 MPa
E_y=8819 MPa	ν_{xz}=0.342	G_{xz}=4315 MPa
E_z=8819 MPa	ν_{yz}=0.380	G_{yz}=3200 MPa

The epoxy-based structural adhesive Araldite® 2015 was considered in this work. A typical stress-strain (σ-ε) curve of the adhesive tested in bulk is presented in Fig. 2 and the properties of the adhesive are detailed in Table 2.

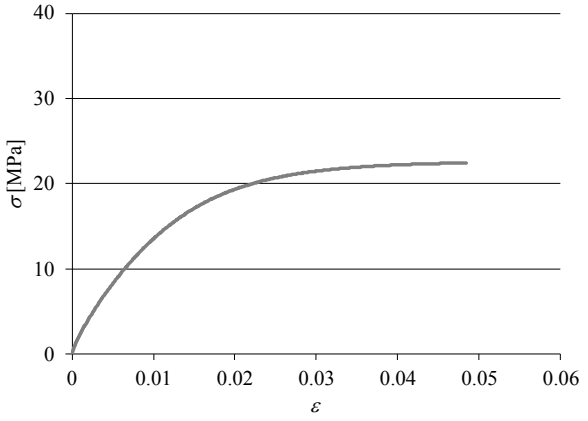

Fig. 2 – Example σ-ε curve of the Araldite® 2015

Table 2 - Properties of the adhesives Araldite® 2015 [19].

Property	2015
Young's modulus, E [GPa]	1.85±0.21
Poisson's ratio, ν	0.33 [a]
Tensile yield stress, σ_y [MPa]	12.63±0.61
Tensile failure strength, σ_f [MPa]	21.63±1.61
Tensile failure strain, ε_f [%]	4.77±0.15
Shear modulus, G [GPa]	0.56±0.21
Shear yield stress, τ_y [MPa]	14.6±1.3
Shear failure strength, τ_f [MPa]	17.9±1.8
Shear failure strain, γ_f [%]	43.9±3.4
Toughness in tension, G_{IC} [N/mm]	0.43±0.02
Toughness in shear, G_{IIC} [N/mm]	4.70±0.34

[a] manufacturer's data

This adhesive was previously characterized [19]. The adhesive properties were obtained through experimental tests, in which the tensile data was obtained by bulk tests to dogbone specimens, and the shear properties were evaluated by Thick Adherend Shear Tests (TAST). Fabrication of the dogbone samples for the tensile tests was consistent with the French standard NF T 76-142 to obtain the samples free of voids. In the TAST tests, the samples were manufactured in accordance with the ISO 11003-2: 1999 standard, for which the adherends were made of DIN C45E steel and the adhesive joints assembled in a mould for alignment during curing. Full details of this procedure are given in reference [20]. Regarding the fracture properties, the Double-Cantilever Beam (DCB) test was used to obtain the tensile fracture energy (G_{IC}) and the End-Notched Flexure (ENF) test was used to estimate the shear fracture energy (G_{IIC}, or in three-dimensions G_{IIC} for shear and G_{IIIC} for tearing). All properties in this work relate to room temperature (20ºC), and are only valid for this condition, since known variations take place with temperature.

3. Numerical analysis

3.1. Pre-processing

Two-dimensional *T*-stiffeners were modelled in Abaqus®, in order to perform a stress analysis to the adhesive layer and strength prediction by CZM, considering the static loading case. As far as the adherends are concerned, these have been modelled with interlaminar and intralaminar layers to create the respective failure mode possibility. Four-node cohesive elements (COH2D4 in the Abaqus library) were used for the interlaminar layers, intralaminar layers and adhesive layer. The adherends were modelled with orthotropic 4-node plain-strain elements (CPE4) [21]. Although generally the mesh was defined as structured, for the deltoid zone, the mesh has a free configuration and predominantly quadratic geometry. The mesh has two types of refinement, one for CZM strength prediction, and another for the study of stresses, which is ten times more refined, to accuracy capture the expected stress gradients at the ends of the overlap area (Fig. 3).

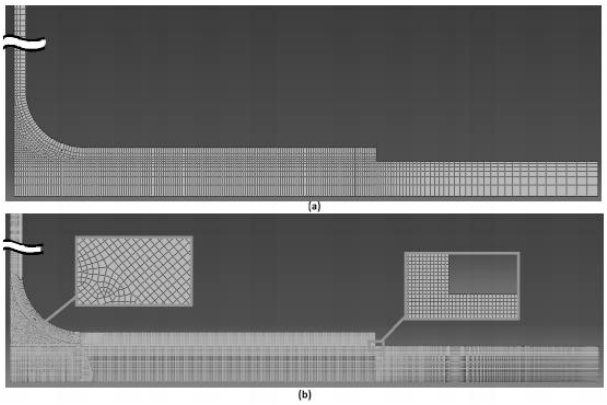

Fig. 3 – Different mesh refinements: CZM (a) and stress analyses (b).

To solve the problem of mesh agreement between the intersection zone of the interlaminar layers and the deltoid ends, it was necessary to remove part of the cohesive material (Fig. 4). The influence of the material removed from the simulation on the final results is considered to be negligible. The locations for possible interlaminar and intralaminar failures in the numerical model are presented in Fig. 5. Six layers have been created, one so-called deltoid curve layer and the others numbered from 1 to 5. The deltoid layer 1 and the deltoid curve layer are 0.125 mm thick, while the remaining layers are 0.02 mm thick. These deltoid failure paths are highly

relevant because of decohesion possibility between the deltoid and parent structure.

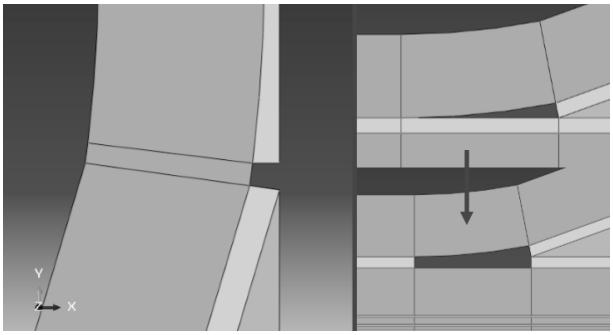

Fig. 4 – Material removal sections

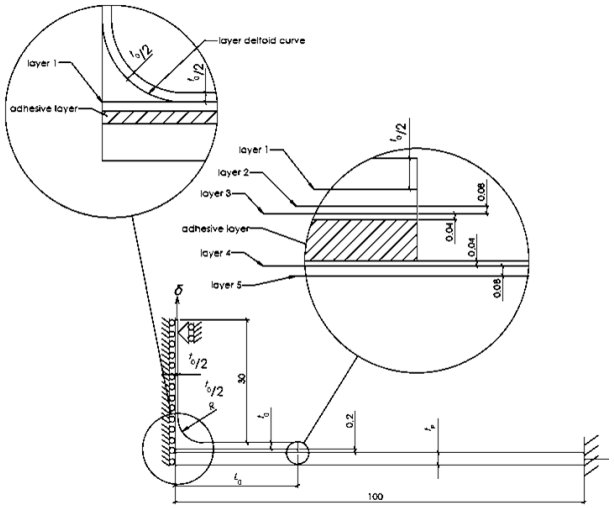

Fig. 5 – Interlaminar, intralaminar and deltoid layers in the numerical models.

Since the composites are anisotropic, it is necessary to establish the fibre orientation in the respective partitions of the numerical models. While the adherend skin has a horizontal fibre orientation, the *T* adherend has a more complex orientation. The layers along the horizontal portion of the *T* are oriented horizontally, and the deltoid portions follow the geometry curvature up to reaching verticality, and this orientation is kept vertical along the *T* adherend. Finally, the boundary conditions applied to the structure consisted of clamping on one end of the adherends, applying a vertical displacement at the top of the *T* reinforcement and inducing symmetry at the vertical mid-plane of the structure.

3.2. CZM theory

CZM are based on relationships between stresses and relative displacements connecting homologous nodes of the cohesive elements, usually addressed as CZM laws. These laws simulate the elastic behaviour up to a peak load and subsequent softening, to model the gradual degradation of material properties up to complete failure. The areas under the traction-separation laws in each mode of loading (tension and shear) are equalled to the respective value of fracture toughness (G_C). Under pure mode, damage propagation occurs at a specific integration point when the stresses are released in the respective traction-separation law. Under mixed mode, energetic criteria are often used to combine tension and shear [12]. In this work, triangular pure and mixed-mode laws, i.e. with linear softening, were considered for the analysis (Fig. 6). The elastic behaviour of the cohesive elements up to the tipping tractions is defined by an elastic constitutive matrix relating stresses and strains across the interface, containing the Young's modulus (E) and the shear modulus (G_{xy}) as main parameters. Damage initiation under mixed-mode can be specified by different criteria. In this work, the quadratic nominal stress criterion was considered for the initiation of damage. After the cohesive strength in mixed-mode (t_m^0) is attained, the material stiffness is degraded. Complete separation is predicted by a linear power law form of the required energies for failure in the pure modes. For full details of the presented model, the reader can refer to reference [22]. The properties of the adhesive for the simulations were taken from Table 2, and the interlaminar and intralaminar properties of the composite are given in a former reference [23]. It should be mentioned that the CZM technique was formerly extensively validated by the authors, including peel-dominant geometries such as *T*-joints [24] and *L*-joints [25]. Moreover, this CZM is valid for the static loading case. For fatigue loading, adaption would be required to account for degradation of the CZM laws with the cyclic count, as described in different available models in the literature.

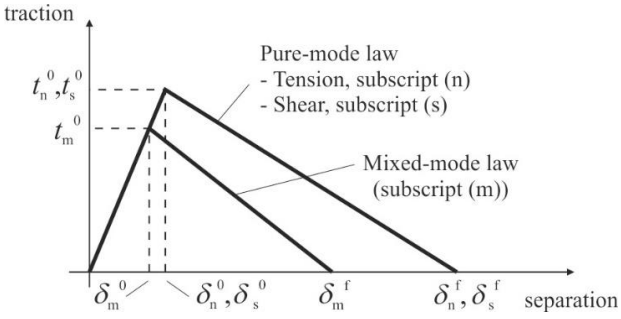

Fig. 6 – Traction-separation law with linear softening law available in Abaqus®.

4. Numerical results

This section includes a parametric analysis to four relevant geometric parameters, which have a significant influence on the stress distributions in the adhesive layer: t_P, t_0, L_O, and R. Thus, the following analysis firstly presents the variations of stress distributions for chosen quantities of each of the mentioned parameters, starting with the base geometry presented in section 2.1, and then the respective joint strength analysis follows.

4.1. Stress analysis

Fig. 7 gives a general overview of peel (σ_y) stresses at the overlap region for the model with base dimensions described

in Section 2.1., showing major stress concentrations at the adhesive tip.

Fig. 7 – General overview of σ_y stresses for the base geometry.

For the detailed stress analysis, σ_y and shear stresses (τ_{xy}) are evaluated, in the elastic loading stage, at the adhesive mid-thickness. It should be mentioned that, for an easy comparison within each studied parameter, both σ_y and τ_{xy} stresses are normalized over the average σ_y ($\sigma_{y\,avg}$) for the respective joint configuration. Moreover, the adhesive length is divided by L_O, such that x/L_O=0 represents the stiffener tip at the beginning of the adhesive layer, and x/L_O=1 corresponds to half the adhesive layer's length (Fig. 1).

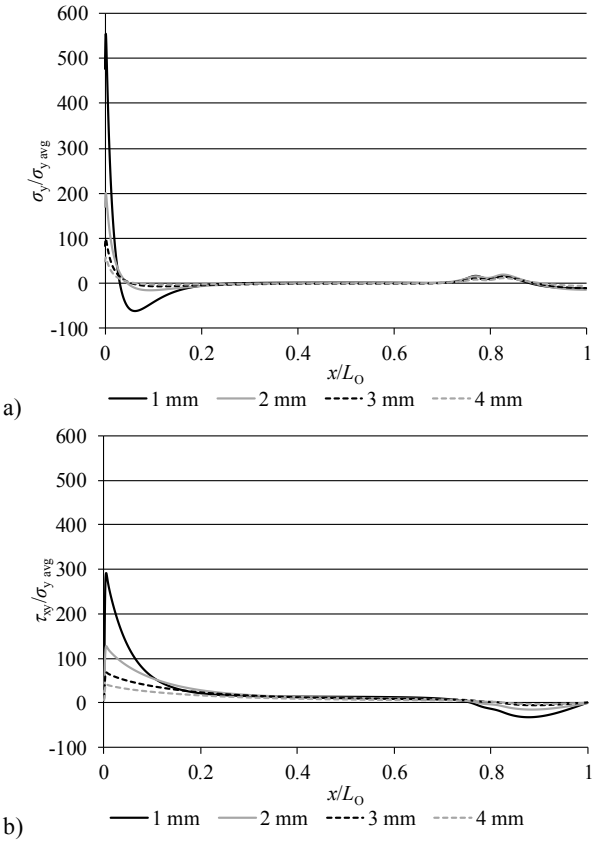

Fig. 8 – σ_y (a) and τ_{xy} (a) stresses distributions in the adhesive layer for the t_P study.

Fig. 8 presents σ_y (a) and τ_{xy} (a) stress distributions in the adhesive layer as a function of t_P. σ_y stresses show essentially a region of major peak stresses at x/L_O=0, whilst the remaining portion of the adhesive is typically unloaded. However, a slight disruption exists at the deltoid region due to the different stiffness between joint constituents. The σ_y peak stresses found at x/L_O=0 are mainly caused by the natural deflexion of the base adherend, which is then counteracted by the tips of the stiffener, causing highly concentrated σ_y peak stresses. A significant difference in overall behaviour was found between different t_P, mainly in the relative σ_y peak stresses in the vicinity of x/L_O=0, which highly increase by reducing t_P. The $\sigma_y/\sigma_{y\,avg}$ peak stresses attain a maximum of 554.3, 199.3, 98.5, and 58.1 for increasing t_P between 1 and 4 mm. This marked increase of peak stresses with the t_P reduction is caused by stiffness reduction and increased rotation at the overlap tips, which tend to increase the peeling effect at this region instead of cleavage that occurs for higher t_P, and corresponding load transfer along a higher extent of adhesive. τ_{xy} stresses are smaller in magnitude to σ_y stresses, but they qualitatively follow the same behaviour, peaking near x/L_O=0, but now with a larger extent across the overlap. τ_{xy} stresses take place because of shearing arising from the overlap rotation due to the base adherends' deformation, which cancels the pure peeling assumption. The peak $\tau_{xy}/\sigma_{y\,avg}$ reduced from 292.1 to 42.4 by increasing t_P from 1 to 4 mm. From this analysis, it is evident that higher t_P should definitely improve the joint strength.

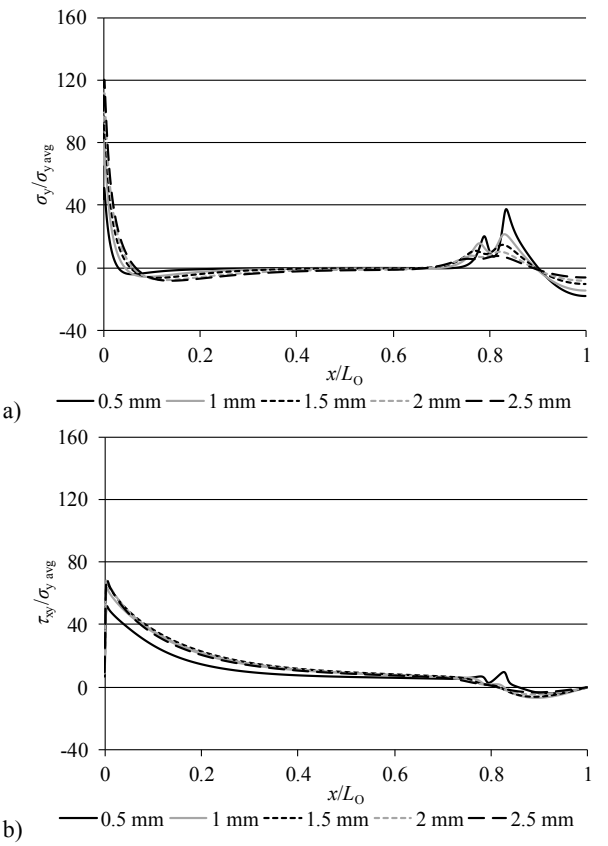

Fig. 9 – σ_y (a) and τ_{xy} (a) stresses distributions in the adhesive layer for the t_0 study.

Fig. 9 reports to σ_y (a) and τ_{xy} (b) stresses for the different t_0. It is visible that both stress components follow the same pattern as previously described, and also that t_0 has much lesser effect on stress distributions than t_P, for the chosen range of this parameter. Actually, σ_y peak stresses only slightly diminished with the t_0 reduction, although this behaviour was expected due to the stiffener's stiffness reduction, which facilitates it to conform to the deformed shape of the base plate. The peak σ_y were 50.8, 79.4, 97.7, 111.7 and 120.3 from t_0=2.5 to 0.5 mm. Whilst stresses are practically nil along the inner overlap, small variations were also found near the deltoid, with emphasis to the smaller t_0, for which peaks of non-negligible magnitude were found. On the other hand, τ_{xy} stresses seem to be even less affected by t_0, except for extremely small values, such as 0.5 mm. $\tau_{xy}/\sigma_{y\,avg}$ peak stresses were 51.6, 64.0, 67.7, 69.6, and 69.6 for t_0 between 0.5 and 2.5 mm. Thus, small t_0 tend to induce peeling closer to x/L_O=1 rather than 0, thus cancelling the shear effect that otherwise would be more significant. This analysis seems to indicate that small t_0 should perform better in this joint configuration.

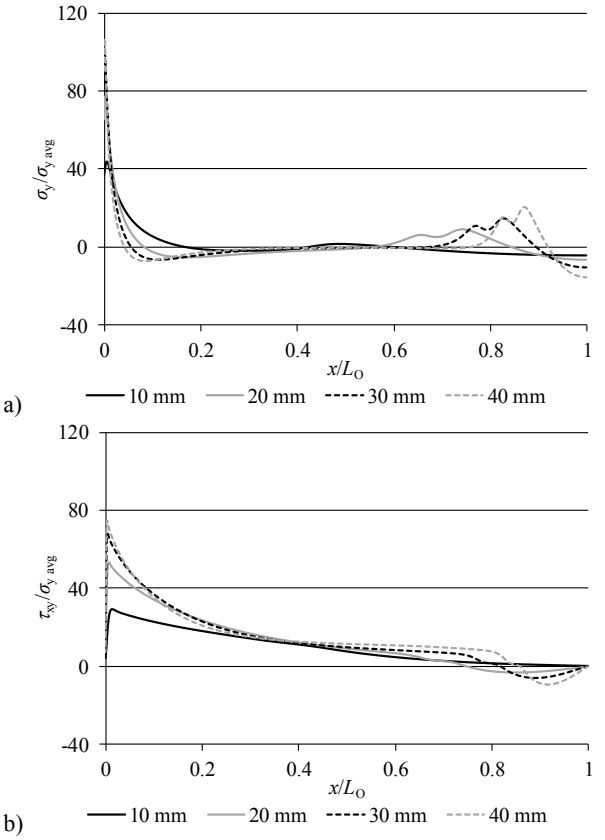

Fig. 10 – σ_y (a) and τ_{xy} (a) stresses distributions in the adhesive layer for the L_O study.

The obtained σ_y (a) and τ_{xy} (b) plots for the L_O study are presented in Fig. 10. It should be emphasized that higher L_O theoretically improve P_m because of increasing the bonding area. However, this is highly affected by variations of peak stresses. The σ_y stress analysis shows that higher L_O increase $\sigma_y/\sigma_{y\,avg}$ by a significant amount. The maximum values of $\sigma_y/\sigma_{y\,avg}$ were 43.8, 77.5, 98.5 and 107.0 for increasing L_O between 10 and 40 mm. Thus, a depreciation of the joint behaviour takes place, which can negatively affect P_m for higher L_O. Minor σ_y peak stresses appear near the deltoid, with a marked tendency to increase in magnitude for higher L_O (up to 144.3% for L_O=40 mm). The τ_{xy} stress analysis reveals the same tendency, i.e., higher τ_{xy} peak stresses by increasing L_O, with an apparent tendency to stabilize for higher L_O. For $\tau_{xy}/\sigma_{y\,avg}$ stresses, the peak values range from 29.3 (L_O=10 mm) to 74.7 (L_O=40 mm), constituting a percentile increase of 154.9%.

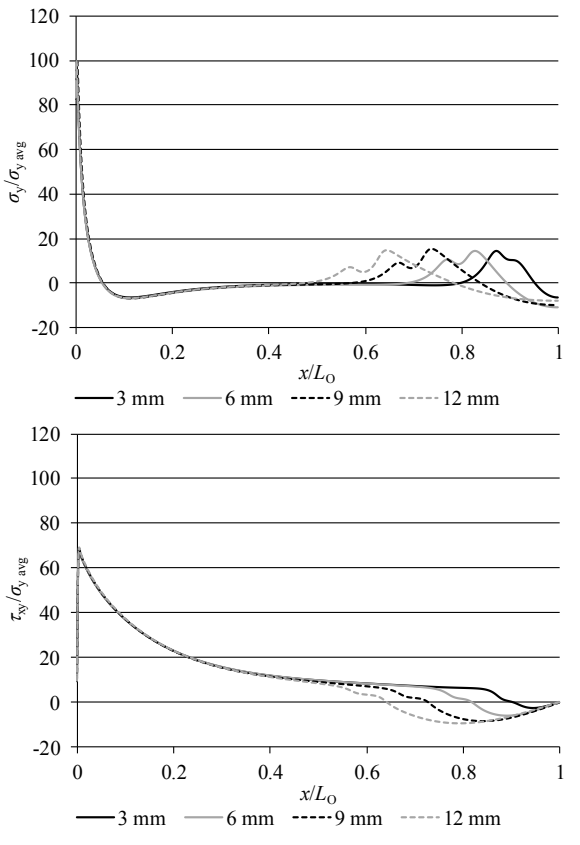

Fig. 11 – σ_y (a) and τ_{xy} (a) stresses distributions in the adhesive layer for the R study.

The influence of R on the stress distributions is shown in Fig. 11 (a) for σ_y and (b) for τ_{xy} stresses. The analysis of σ_y stresses shows that no visible modification arises at the critical region (x/L_O=0) by changing R. Although no major difference takes place regarding the magnitude of σ_y stresses, the disruption in the stress plots tends to follow the deltoid size and extent in the adhesive layer. The same conclusion can be taken from τ_{xy} stresses, in which stresses at x/L_O=0 are virtually equal between all R. Equally to σ_y stresses, higher R tend to induce a modification to τ_{xy} stresses that is longer in length. As a result of this discussion, it is hypothesized that R should have a small effect on P_m.

4.2. Joint strength

This section presents the results of the parametric study on the joint strength, divided into four analyses: t_P, t_0, L_O and R (Fig. 12). It should be mentioned that, despite introducing several failure mode possibilities, failures were essentially cohesive in the adhesive layer, although in some cases with partial or total deltoid detachment.

Fig. 12 (a) shows the P_m-t_P results. Increasing t_P mostly increases P_m, although this behaviour is cancelled between t_P=2 and 3 mm, inclusively with a short P_m reduction of approximately 1.3%. The percentile improvements of P_m using as reference t_P=1 mm were 63.3% for t_P=2 mm, 61.1% for t_P=3 mm and 94.1% for t_P=4 mm. This result was highly anticipated from the former stress analysis, due to the major σ_y and τ_{xy} reduction occurring from increasing t_P. Actually, the improved stiffness of the base adherend has an important effect in spreading stresses in the adhesive layer over a bigger area, which translates into an improved P_m. Although it is not presented here, partial deltoid detachment was found for $t_P \geq 3$ mm, which justifies the loss of P_m for higher t_P.

The P_m results for the t_0 study are presented in Fig. 12 (b). Here, the tendency is opposite to t_P, since P_m significantly reduces between t_0=0.5 mm and t_0=1mm. However, the P_m values for t_0 between 1 and 2.5 mm remained close. The percentile reductions of P_m, using t_0=0.5 mm as reference, were: 22.1% for t_0=1 mm, 20.1% for t_0=1.5 mm, 26.6% for t_0=2 mm and 27.3% for t_0=2.5 mm. As discussed in Section 4.1, the reduction of t_0 induces a higher compliance of the stiffener and locally reduces peak stresses. This effect was particularly visible for σ_y stresses, while for τ_{xy} a noteworthy difference in the stress plots was only observed for t_0=0.5 mm, whilst the difference between the other t_0 was negligible. It should also be emphasized that the cohesive failure of the adhesive was accompanied by failure at the deltoid region for $t_0 \leq 1.5$ mm, which could have limited P_m for these joint configurations. L_O is one of the parameters that traditionally influences the most P_m of adhesive joints due to changing the bonding area.

The results of the P_m-L_O analysis are presented in Fig. 12 (c). In this analysis, P_m increases between L_O=10 and 20 mm, but then it reduces gradually up to reaching a minimum for L_O=40 mm. The percentile P_m improvements using as reference L_O=10 mm were 30.5% for L_O=20 mm and 9.7% for L_O=30 mm, but then a 20.1% reduction occurs for L_O=40 mm.

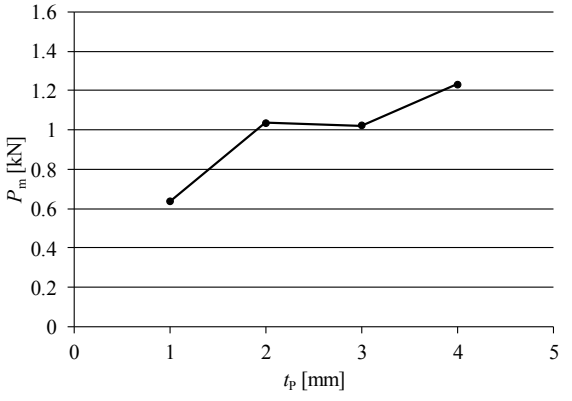

a)

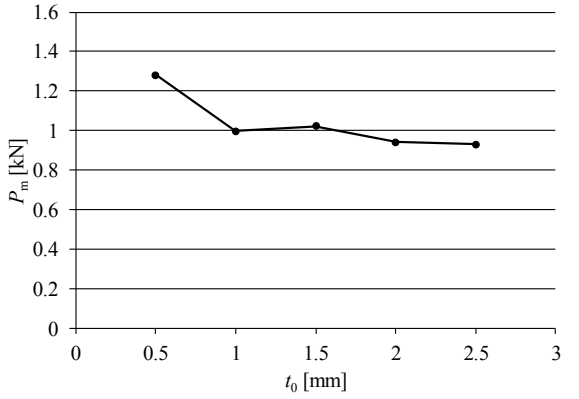

b)

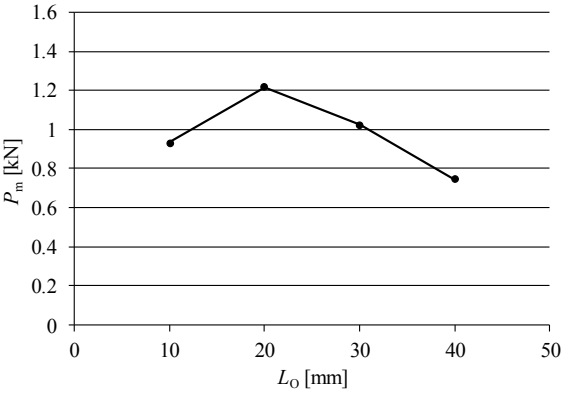

c)

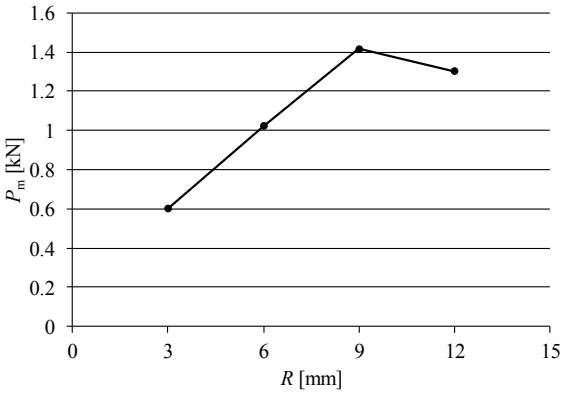

d)

Fig. 12 – P_m as function of t_P (a), t_0 (b) L_O (c) and R (d).

It was formerly shown that higher L_O tend to increase both σ_y and τ_{xy} peak stresses, which counteracts the positive effect of higher adhesive area resisting separation. In this analysis, it was verified that cohesive failures of the adhesive took place for L_O=10 and 20 mm but, above this L_O, major premature deltoid failure prevented higher loads to be attained, and this resulted in a performance loss. However, and contradicting expected results for conventional joint geometries such as single-lap joints, the modification of the failure paths highly affected P_m.

The P_m-R numerical results are depicted in Fig. 12 (d), showing higher performance for bigger R, although with a short reduction from R=3 to 4 mm. The percentile P_m improvements

over R=3 mm were: 69.9% for R=6 mm, 135.4% for R=9 mm and 116.4% for R=12 mm. The former σ_y and τ_{xy} stress analyses showed no relevant modifications of the peak stresses at the stiffener tips by changing R, but higher loads are transferred between the base laminate and the stiffener at the deltoid region as its dimensions are increased, which justifies the respective P_m improvement. The failure modes included deltoid damage accompanying failure of the adhesive layer for lower R and fully cohesive failure of the adhesive for higher R, which reinforces the obtained results.

5. Conclusions

The present work aimed to study, by CZM, the behaviour of adhesively-bonded *T*-stiffeners in CFRP structures, considering different geometries (t_P, t_0, L_O and R), and the adhesive Araldite® 2015. The effect of the different parameters is as follows:

- Considering different t_P, it was observed that σ_y stresses peak at x/L_O=0, while the rest of the adhesive is typically unloaded. σ_y peak stresses considerably increased by reducing t_P. τ_{xy} stresses are smaller than σ_y stresses, but they also peak close to x/L_O=0. As a result of these differences, P_m increased by 94.1% from t_P=1 and 4 mm;
- t_0 has much less effect on stress distributions than t_P, taking into account the chosen values for this parameter. Nonetheless, σ_y and τ_{xy} peak stresses slightly decreased for smaller t_0, which was expected due to the stiffener's stiffness reduction. As a result of this stress reduction, P_m significantly increases for t_0=0.5 mm. The P_m reduction between t_0=0.5 and 2.5 mm was 27.3%;
- The increase of L_O promotes a significant aggravation of σ_y and τ_{xy} normalized stresses. Thus, just on account of this effect, P_m would be reduced. However, the higher bonding areas end up by counteracting this effect and, effectively, between L_O=10 and 20 mm, P_m increases by 30.5%. However, above this L_O premature deltoid failure took place, which cancelled this effect;
- R only locally affects load transfer near the deltoid. On the other hand, no difference was found on σ_y and τ_{xy} stresses near to x/L_O=0, where the other geometrical modifications are highly influent. However, higher R lead to higher loads being transferred between the base laminate and the stiffener at the deltoid region, which justifies the respective P_m improvement, up to 135.4% between R=1 and 3 mm.

References

[1] R.D. Adams. Adhesive bonding: science, technology and applications. Cambridge: Woodhead Publishing Limited; 2005.
[2] A.V. Pocius. Adhesion and adhesives technology: an introduction: Carl Hanser Verlag GmbH Co KG; 2012.
[3] L.F.M. da Silva, A.G. de Magalhaes, M.F.S. de Moura. Juntas adesivas estruturais: Publindústria; 2007.
[4] L.F. Da Silva, A. Öchsner, R.D. Adams. Handbook of adhesion technology: Springer Science & Business Media; 2011.
[5] X. He, A review of finite element analysis of adhesively bonded joints, International Journal of Adhesion and Adhesives 2011;31:248-64.
[6] A. Mubashar, I.A. Ashcroft, A.D. Crocombe, Modelling damage and failure in adhesive joints using a combined XFEM-cohesive element methodology, The Journal of Adhesion 2014;90:682-97.
[7] L.F.M. da Silva, P.J.C. das Neves, R.D. Adams, J.K. Spelt, Analytical models of adhesively bonded joints—Part I: Literature survey, International Journal of Adhesion and Adhesives 2009;29:319-30.
[8] S. Akpinar, The strength of the adhesively bonded step-lap joints for different step numbers, Composites Part B: Engineering 2014;67:170-8.
[9] J.D. Clark, I.J. McGregor, Ultimate Tensile Stress over a Zone: A New Failure Criterion for Adhesive Joints, The Journal of Adhesion 1993;42:227-45.
[10] J.-Q. Xu, Y.-H. Liu, X.-G. Wang, Numerical methods for the determination of multiple stress singularities and related stress intensity coefficients, Engineering Fracture Mechanics 1999;63:775-90.
[11] R.D.S.G. Campilho, M.F.S.F. de Moura, A.M.J.P. Barreto, J.J.L. Morais, J.J.M.S. Domingues, Experimental and numerical evaluation of composite repairs on wood beams damaged by cross-graining, Construction and Building Materials 2010;24:531-7.
[12] G. Alfano, On the influence of the shape of the interface law on the application of cohesive-zone models, Composites Science and Technology 2006;66:723-30.
[13] M. Heidari-Rarani, M.M. Shokrieh, P.P. Camanho, Finite element modeling of mode I delamination growth in laminated DCB specimens with R-curve effects, Composites Part B: Engineering 2013;45:897-903.
[14] S. Mohammadi. Extended Finite Element Method: for Fracture Analysis of Structures: Wiley; 2008.
[15] J.C.S. Azevedo, R.D.S.G. Campilho, J.F.G. da Silva, T.M.S. Faneco, R.M. Lopes, Cohesive law estimation of adhesive joints in mode II condition, Theoretical and Applied Fracture Mechanics 2015;80:143-54.
[16] S.T. de Freitas, J. Sinke, Failure analysis of adhesively-bonded skin-to-stiffener joints: Metal–metal vs. composite–metal, Engineering Failure Analysis 2015;56:2-13.
[17] R. Shenoi, F. Violette, A study of structural composite tee joints in small boats, Journal of composite materials 1990;24:644-66.
[18] F. Ribeiro, R. Campilho, R. Carbas, L. Da Silva, Strength and damage growth in composite bonded joints with defects, Composites Part B: Engineering 2016;100:91-100.
[19] R.D. Campilho, M.D. Banea, J. Neto, L.F. da Silva, Modelling adhesive joints with cohesive zone models: effect of the cohesive law shape of the adhesive layer, International Journal of Adhesion and Adhesives 2013;44:48-56.
[20] R.D.S.G. Campilho, A.M.G. Pinto, M.D. Banea, R.F. Silva, L.F.M. da Silva, Strength Improvement of Adhesively-Bonded Joints Using a Reverse-Bent Geometry, Journal of Adhesion Science and Technology 2011;25:2351-68.
[21] R.D. Campilho, M.D. Banea, A.M. Pinto, L.F. da Silva, A. De Jesus, Strength prediction of single-and double-lap joints by standard and extended finite element modelling, International Journal of Adhesion and Adhesives 2011;31:363-72.
[22] R.D.S.G. Campilho, M.D. Banea, J.A.B.P. Neto, L.F.M. da Silva, Modelling of single-lap joints using cohesive zone models: Effect of the cohesive parameters on the output of the simulations, The Journal of Adhesion 2012;88:513-33.
[23] J.A.B.P. Neto, R.D.S.G. Campilho, L.F.M. da Silva, Parametric study of adhesive joints with composites, International Journal of Adhesion and Adhesives 2012;37:96-101.
[24] M.A.S. Carneiro, R.D.S.G. Campilho, Analysis of adhesively-bonded T-joints by experimentation and cohesive zone models, Journal of Adhesion Science and Technology 2017;31:1998-2014.
[25] N.R.E. Domingues, R.D.S.G. Campilho, R.J.C. Carbas, L.F.M. da Silva, Experimental and numerical failure analysis of aluminium/composite single-L joints, International Journal of Adhesion and Adhesives 2016;64:86-96.